

**X-ray diffraction peaks from partially ordered misfit dislocations**

Vladimir M. Kaganer

*Paul-Drude-Institut für Festkörperelektronik, Hausvogteiplatz 5-7, 10117 Berlin, Germany*

Karl K. Sabelfeld

*Institute of Computational Mathematics and Mathematical Geophysics, Russian Academy of Sciences,  
Lavrentiev Prosp. 6, 630090 Novosibirsk, Russia*

(Received 17 August 2009; revised manuscript received 19 October 2009; published 11 November 2009)

We calculate the x-ray diffraction peak profiles from distributions of misfit dislocations in the whole range of their positional correlations, from completely random to periodic. Both the spatial integration and the integration over the dislocation ensemble are performed by Monte Carlo techniques. The diffraction peaks from thin relaxed films consisting of a narrow coherent and a broad diffuse component are explained. Correlation functions are calculated analytically for different types of positional correlations between dislocations.

DOI: [10.1103/PhysRevB.80.184105](https://doi.org/10.1103/PhysRevB.80.184105)

PACS number(s): 61.05.cp, 68.35.-p, 61.72.Dd, 61.72.Lk

**I. INTRODUCTION**

Epitaxial growth of a film with lattice parameters different from the ones of the substrate gives rise to elastic strain in the film. The accumulated elastic strain energy is proportional to the film thickness and is released at some stage either plastically, through the introduction of dislocations, or elastically, by the formation of surface undulations or three-dimensional islands. The elastic relaxation can sufficiently reduce the strain energy only in rather thin films, so that further deposition leads to plastic relaxation. As a result, sufficiently thick mismatched epitaxial films are plastically relaxed by networks of dislocations located at the film-substrate interface (misfit dislocations).

Plastic relaxation proceeds differently in systems with small and large misfits (let us say, below and above 1%). If the misfit is small, a smooth strained dislocation-free layer grows first. Dislocations reduce the elastic energy only after the thickness exceeds some critical value. The critical thickness can be calculated either by considering elastic forces acting on the dislocation,<sup>1</sup> or by comparing the elastic energies of the films with and without dislocations.<sup>2</sup> The energetics and the relaxation kinetics of films with small mismatch are well-studied, both theoretically and experimentally (see, e.g., the reviews).<sup>3,4</sup> The dislocations nucleate at the film surface and glide through the film to the interface. Since their glide planes are inclined with respect to the interface, they cannot move along the interface to further reduce the elastic energy. The positions of the misfit dislocations are determined by the dislocation sources at the surface.

In systems with large misfit, the critical thickness decreases to just a few, or even less than one, atomic layer. Misfit dislocations are introduced from the edges of small three-dimensional islands before islands coalesce, or they even form at the interface together with the nucleating island. These dislocations are usually edge dislocations with a Burgers vector in the interfacial plane (Lomer-type dislocations). Such dislocations most efficiently release the elastic strain and, at the same time, can glide along the interface. Since a periodic dislocation array realizes the lowest energy state for a given dislocation density, Lomer dislocations tend to arrange periodically. Let us also mention, for the sake of

completeness, the case of very large misfit (let us say, larger than 10%). In such systems, a coincidence lattice, rather than misfit dislocations, forms at the interface (see, e.g., Ref. 5 and references therein). We do not consider this case in the present paper.

X-ray diffraction is commonly used to detect plastic relaxation in heteroepitaxial systems. The degree of relaxation and hence the misfit dislocation density is determined directly from the relative positions of the film and the substrate peaks.<sup>6-8</sup> The information on the dislocation distribution that is contained in the peak profiles, however, relatively rarely becomes the subject of study.

The x-ray diffraction peak profiles from epitaxial films with misfit dislocations<sup>9</sup> differ from the diffraction peaks of bulk dislocated crystals.<sup>10,11</sup> The coherent peak is present even for positionally uncorrelated misfit dislocations, while it is absent for dislocations in bulk crystals. This is a result of the elastic strain relaxation at the free film surface. The long-range component of the dislocation strain, which decays as  $r^{-1}$  (where  $r$  is the distance from the dislocation), is compensated by the image dislocation, similarly to the electrostatic problem of a charge placed at some distance from a conductive plane. Since the dislocation makes a dipole with its image dislocation, the strain due to a dislocation parallel to the free surface decays as  $r^{-2}$ , the Debye-Waller factor remains finite, and the coherent peak survives. For uncorrelated misfit dislocations, however, the coherent peak can practically be observed only if the mean distance between dislocations is large compared to the film thickness.<sup>9</sup>

The correlations between dislocations in bulk crystals act to reduce the elastic energy of the crystal by screening the dislocation strain field by surrounding dislocations.<sup>12-14</sup> Similar screening is characteristic for threading dislocations in epitaxial films.<sup>15-17</sup> The driving force for correlations between misfit dislocations is quite different. They do not screen each other but produce the collective effect to release mismatch. Their correlations are directed to minimize the energy of the system by developing a periodic dislocation array. Periodic arrays of misfit dislocations have been proven to exist in several systems<sup>18-24</sup> by the presence of satellite peaks.

The diffraction peaks calculated for large densities of uncorrelated misfit dislocations are notably broader than the experimentally observed peaks.<sup>9</sup> A correction to pair correlations between the dislocations was proposed by assuming that the mean distance between dislocations is much smaller than the correlation length which, in turn, is much smaller than the film thickness. Large correction factors were required to quantitatively describe the experiments. On the other hand, all characteristic features of the diffraction pattern (relative widths of the peaks, orientation of the spots in reciprocal space maps, etc.) were in good agreement with the model of uncorrelated dislocations. An explanation found later by analyzing the GaAs/Si(001) system<sup>25</sup> is that, the misfit dislocation network consists of two parts. The majority of the dislocations are Lomer dislocations that order periodically and do not cause broadening of the diffraction peaks. A smaller number of 60° dislocations glide from the surface and add an uncorrelated distribution at the interface. These dislocations determine the width of the diffraction peak.

Another type of diffraction pattern was found experimentally for epitaxial films with a misfit of a few percent and thicknesses of tens of nanometers. It consists of a narrow central peak accompanied by a broad diffuse background. Such a pattern was observed for various metal,<sup>26–38</sup> semiconductor,<sup>20,21,39,40</sup> oxide,<sup>41–43</sup> and ferroelectric<sup>44–46</sup> epitaxial films. Different authors finally agreed that the misfit dislocations are the source of the two-component profiles. Barabash *et al.*<sup>47</sup> proposed a quantitative treatment of the peaks. They noted that the Debye-Waller factor for misfit dislocations in epitaxial films is not zero, in contrast to the case of dislocations in bulk crystals, and the coherent peak persists. However, a detailed calculation of the coherent peak for uncorrelated misfit dislocations (see Fig. 5 in Ref. 9) shows that the coherent intensity decreases by two orders of magnitude, compared to a dislocation-free film, already for a film thickness equal to the mean distance between dislocations. The coherent intensity decreases exponentially with further increasing the film thickness. This conclusion is confirmed by the calculations below, see the thick (green) line in Fig. 3(a): for uncorrelated dislocations with a mean distance between the dislocations two times smaller than the film thickness, the transverse peak already assumes a Gaussian shape, a coherent peak is absent. The calculations below show that sufficiently strong correlations in the dislocation positions are required to retain the coherent peak.

The aim of the present work is to theoretically investigate the x-ray diffraction peaks arising from misfit dislocation arrays in the whole range of possible order, from completely uncorrelated to nearly periodic. We show that both the statistical average over the dislocation distribution and the spatial integration to obtain the diffracted intensity can be performed by the double randomization Monte Carlo method.<sup>48</sup> We also demonstrate that this method is a powerful tool to calculate x-ray diffraction profiles due to various defect distributions with given statistical properties. We have already presented a brief description of the Monte Carlo method and used it to explain the x-ray diffraction measurements on the GaN epitaxial films.<sup>49</sup>

Recently, Holy *et al.*<sup>50</sup> employed our initial idea of the Monte Carlo calculation of the diffraction peaks. They gen-

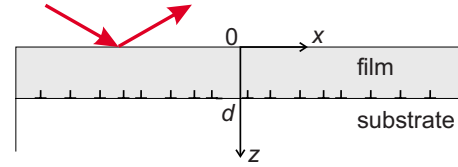


FIG. 1. (Color online) Geometry of the misfit dislocations in a relaxed epitaxial film.

erated just one set of threading dislocations at random and performed the spatial integration by the standard quadratures. Since strongly oscillating functions make numerical integration very difficult, they simplified the spatial integrals using the stationary-point approximation. In the present work, in contrast to Ref. 50, we take into account the correlations in the dislocation positions, perform statistical averaging over the dislocation ensemble, and carry out the spatial integration also by the Monte Carlo method.

The atomic displacements in the epitaxial film are the sums of the displacements caused by the individual dislocations. Since the dislocation displacements only slowly decrease with the distance, a large number of dislocations contribute to the total displacement of a given atom. We find that the total displacements, considered as random functions of the dislocation positions, reach the normal distribution as soon as the mean distance between dislocations is smaller than the film thickness. This allows us to evaluate the diffracted intensity through the correlation function of the dislocation positions. We obtain the correlation functions analytically for a variety of short and long-range correlations.

## II. MONTE CARLO CALCULATION OF THE DIFFRACTED INTENSITY

The diffraction geometry most suited to study arrays of misfit dislocations and commonly used in the experiments is at the same time most suitable one for the intensity calculations, see Fig. 1. We consider an array of dislocations randomly positioned at the film-substrate interface. The scattering plane is the plane of the figure, and the dislocation lines are perpendicular to it. We restrict ourselves to symmetric Bragg reflections, since primarily these reflections are measured experimentally. The calculation method developed below, however, is generic and equally well-suited for any other dislocation arrangement or diffraction geometry. In the common case of a 001 oriented cubic crystal, the dislocation array shown in Fig. 1 completely determines the diffuse intensity in the transverse scans.<sup>9</sup> The second array, with the dislocation lines parallel to the scattering plane, only provides a static Debye-Waller factor.

We consider a half-infinite crystal with the surface  $z=0$  and misfit dislocations located at the interface  $z=d$  between the substrate ( $z>d$ ) and the epitaxial film ( $0<z<d$ ), see Fig. 1. The scattering plane is the  $xz$  plane, the dislocation lines run along the  $y$  axis. The x-ray scattering amplitude from the film is given by the integral

$$A(q_x, q_z) = \int_{-\infty}^{\infty} dx \int_0^d dz \exp\{i[q_x x + q_z z + V(x, z)]\}, \quad (1)$$

where we denote  $V(x, z) = \mathbf{Q} \cdot \mathbf{U}(x, z)$ . Here,  $\mathbf{U}(x, z)$  is the displacement at the point  $(x, z)$  caused by all dislocations,  $\mathbf{Q}$  is

the reciprocal lattice vector, and  $(q_x, q_z)$  are small deviations of the scattering vector from  $\mathbf{Q}$  in the scattering plane, along  $x$  and  $z$  directions, respectively. Equation (1) takes into account that the displacement  $\mathbf{U}(x, z)$  due to dislocations shown in Fig. 1 does not depend on  $y$ . Hence, we omit the integration over  $y$  of the term  $\exp(iq_y y)$ . The intensity calculated below needs to be multiplied with a delta-function  $\delta(q_y)$  originated from this integration. We do not include it in the equations explicitly, since we are interested in the intensity distribution in the scattering plane. The vectors  $\mathbf{Q}$  and  $\mathbf{U}$  are generally three-dimensional vectors. We restrict the calculations below to the symmetric Bragg case,  $\mathbf{Q}=(0, 0, Q)$ , and to edge dislocations with the Burgers vector in the interfacial plane,  $\mathbf{b}=(b, 0, 0)$ . Then, only one component of the displacement vector, namely,  $U_z(x, z)$ , is relevant to the present problem.

The total displacement at a point  $(x, z)$  due to all misfit dislocations is given in linear elasticity theory by the sum  $\mathbf{U}(x, z)=\sum_j \mathbf{u}(x-\xi_j, z)$  of the displacement fields of individual dislocations located at random positions  $\xi_j$  at the interface and running perpendicular to the scattering plane (along the  $y$  axis). We can represent  $V(x, z)$  as a sum

$$V(x, z) = \sum_j v(x - \xi_j, z), \quad (2)$$

where  $v(x, z)=\mathbf{Q} \cdot \mathbf{u}(x, z)$ . The explicit expressions for the displacement  $\mathbf{u}(x, z)$  due to a dislocation parallel to the free surface are well-known.<sup>51</sup> A complete set of expressions for all Burgers vector components is collected in Appendix B of Ref. 9. The displacement component involved in the calculations of the present paper is given in the Appendix to the present paper, see Eqs. (A1)–(A3).

It is also useful for the analysis below to introduce the microscopic dislocation density

$$g(x) = \sum_j \delta(x - \xi_j), \quad (3)$$

where  $\delta(x)$  is the delta function. The mean dislocation density is  $\langle g(x) \rangle = \rho$ . Then,  $V(x, z)$  can be represented by the integral

$$V(x, z) = \int_{-\infty}^{\infty} v(x - \xi, z) g(\xi) d\xi. \quad (4)$$

The scattered intensity is  $\mathcal{I}(q_x, q_z) = \langle |A(q_x, q_z)|^2 \rangle$ , where the angular brackets  $\langle \dots \rangle$  denote the average over statistics of the random positions  $\xi_j$  of the dislocations. The intensity can be written as

$$\mathcal{I}(q_x, q_z) = \int_{-\infty}^{\infty} dx \int \int_0^d dz_1 dz_2 e^{iq_x x + iq_z(z_1 - z_2)} G(x, z_1, z_2), \quad (5)$$

where the function  $G(x, z_1, z_2)$  is given by

$$G(x, z_1, z_2) = \langle \exp\{i[V(x_1, z_1) - V(x_2, z_2)]\} \rangle. \quad (6)$$

We take into account that the system is homogeneous in the  $xy$ -plane, so that only the distance between two points

$x=x_1-x_2$  is relevant. There is no such homogeneity in the  $z$  direction, however.

Both the spatial integration (5) and the average over the dislocation statistics (6) can be performed by a Monte Carlo method: generate a set of dislocations  $\{x_j\}$  according to their distribution, generate a random point  $\{x, z_1, z_2\}$ , and make contributions for all points  $(q_x, q_z)$  of interest. Such a straightforward calculation encounters a difficulty in the integration over the  $x$  coordinate: the function  $G(x, z_1, z_2)$  approaches a finite value in the limit  $x \rightarrow \infty$ , which results in a delta-function  $\delta(q_x)$  in the integral (5). It represents the coherent diffraction peak. The experiment does not suffer from this difficulty because of its finite resolution. We take care of this problem by introducing an appropriate resolution function in the Monte Carlo calculation.

Let us consider a measurement of diffracted intensity (5) with a finite-resolution  $\mathcal{R}(q_x)$ . We take a Gaussian resolution function,

$$\mathcal{R}(q_x) = \frac{\sigma_x}{\sqrt{2\pi}} \exp\left[-\frac{1}{2}(q\sigma_x)^2\right], \quad (7)$$

where  $\sigma_x$  is the real-space resolution (the coherence length). We consider the resolution in the  $x$  direction only. The resolution along  $q_z$  could be introduced in exactly the same way. However, the real-space resolution  $\sigma_x$  used in the calculations below is several times larger than the film thickness  $d$ , so that the introduction of a similar  $z$  resolution does not change the calculated intensity distributions. In other words, we do not need to take into account the  $q_z$  resolution as long as the thickness fringes are resolved in the diffraction pattern.

The finite-resolution intensity distribution is obtained as the convolution

$$I(q_x, q_z) = \int \mathcal{I}(q'_x, q_z) \mathcal{R}(q_x - q'_x) dq'_x. \quad (8)$$

One can proceed from the convolution to the product of the Fourier transforms, since the intensity  $\mathcal{I}(q_x, q_z)$  is already represented by a Fourier integral (5)

$$I(q_x, q_z) = \int_{-\infty}^{\infty} dx \int \int_0^d dz_1 dz_2 \langle J \rangle R(x), \quad (9)$$

where

$$J = e^{i[q_x x + q_z(z_1 - z_2) + V(x_1, z_1) - V(x_2, z_2)]} \quad (10)$$

and  $R(x) = \exp[-\frac{1}{2}(x/\sigma_x)^2]$ .

Let us consider the integration over  $x$  and represent Eq. (9) as

$$\mathcal{I}(q_x, q_z) = \int_{-\infty}^{\infty} F(x) p(x) dx, \quad (11)$$

where

$$F(x) = \sqrt{2\pi}\sigma_x \int \int_0^d dz_1 dz_2 \langle J \rangle. \quad (12)$$

We define  $p(x) = (\sqrt{2\pi}\sigma_x)^{-1}R(x)$ , so that  $p(x)$  is normalized,  $\int_{-\infty}^{\infty} p(x)dx = 1$ . One can treat  $p(x)$  as a probability density. Then, the integral (11) is the function  $F(x)$  averaged over the probability density  $p(x)$ . The Monte Carlo calculation of this integral consists in the summation of the values  $F(x)$  at the points  $x$  chosen according to the distribution  $p(x)$ . Since our resolution function is Gaussian (7), we can generate random points  $x$  possessing a Gaussian distribution with the well-established and efficient algorithms and codes.<sup>52</sup>

The Monte Carlo estimate of the intensity (9) is the sum

$$I(q_x, q_z) = \frac{\mathcal{V}}{N} \sum_{n=1}^N J_n, \quad (13)$$

where  $N$  is the number of generated configurations  $n = (x, z_1, z_2, \{\xi_j\})$  and  $J_n$  is the value of  $J$  calculated for a configuration  $n$  by Eq. (10). A ‘‘coherence volume’’  $\mathcal{V}$  is defined as  $\mathcal{V} = \sqrt{2\pi}\sigma_x d^2$ . The values of  $z_1$  and  $z_2$  are uniformly distributed from 0 to  $d$ , the values of  $x$  possess a Gaussian distribution with the dispersion  $\sigma_x$ , and the dislocations are positioned at  $\{\xi_j\}$  according to the physical model of their correlations. We explore several models of dislocation distributions in the next sections.

The accuracy of the approximation that replaces the integral (9) by the finite sum (13) is given by the statistical error,  $\pm \sigma_I / \sqrt{N}$ , in which the dispersion  $\sigma_I^2$  can be estimated as

$$\sigma_I^2 = \mathcal{V}^2 \left[ \frac{1}{N} \sum_{n=1}^N J_n^2 - \left( \frac{1}{N} \sum_{n=1}^N J_n \right)^2 \right]. \quad (14)$$

The two sums, the ones of  $J_n$  and  $J_n^2$ , can be accumulated in parallel without extra computational effort. We also found it useful to calculate both the real and imaginary parts of the sum (13). Since the intensity is a real quantity, the imaginary part is of the same order as the statistical error and decreases as the number  $N$  of the generated configurations increases. Equations (13) and (14) are ideally suited for parallel computation: different parts of the sums can be independently calculated and combined at the end.

### III. CALCULATION RESULTS

In this section, we apply the Monte Carlo method to calculate diffraction peak profiles for plausible models of dislocation distributions. We find that the experimentally observed peaks in different epitaxial systems can be explained by these distributions.

We consider mean distances between dislocations comparable to the film thickness  $d$ . A decorrelation of the dislocation positions is expected at distances exceeding  $d$ . As the simplest model, we assume that, once the position  $\xi_j$  of the dislocation is specified, the position of the next dislocation is  $\xi_{j+1} = \xi_j + \delta x$ , where the random increment  $\delta x$  does not depend on the number  $j$ . Its mean is equal to the average distance between dislocations,  $\langle \delta x \rangle = \rho^{-1}$ , where  $\rho$  is the linear dislocation density. In this model, the positions of the dislo-

cations form a Markov chain, which allows an analytical calculation of the correlation function, see Sec. V A. It is convenient to take the gamma distribution

$$p(x) = \frac{\gamma \rho (\gamma \rho x)^{\gamma-1} e^{-\gamma \rho x}}{\Gamma(\gamma)} \quad (15)$$

to model the dislocation distances. Here,  $\Gamma(\gamma)$  is the gamma function and  $\gamma$  is a parameter that allows a smooth transition from the case of random uncorrelated dislocations with an exponential probability distribution at  $\gamma=1$  to the case of periodic dislocations at  $\gamma \rightarrow \infty$ . For  $\gamma \gg 1$ , the distribution (15) has a bell-shaped peak centered at  $\bar{x} = \rho^{-1}$  with a half-width proportional to  $\gamma^{-1/2}$ . Efficient algorithms and codes to generate random numbers possessing a gamma distribution are readily available.<sup>52</sup>

Figure 2 illustrates Monte Carlo calculations of the integral (9). First, we generate a set of dislocations as a Markov chain with the gamma distribution of distances between subsequent dislocations and a given dislocation density  $\rho$ . Then, we generate the points  $z_1$  and  $z_2$ , uniformly distributed over  $[0, d]$ , and the point  $x$  possessing the Gaussian distribution with the dispersion  $\sigma_x$  chosen as the spatial resolution. The term (10) is calculated for a predefined set of values  $(q_x, q_z)$  that are of interest and added to the sums (13) and (14) to calculate the mean value of intensity and the error, respectively. The spatial integration over  $x$ ,  $z_1$ , and  $z_2$  and the statistical average over the dislocation distribution  $\{x_j\}$  are independent. Since the random number generation takes about half of the computation time, the generation of a new dislocation distribution for every spatial point is not efficient. We use the dislocation distribution, once generated, for a number of spatial points roughly equal to the number of dislocations (which varies from hundreds to thousands).

Figure 2(a) presents a  $q_z$  scan of the intensity at  $q_x=0$  calculated by the Monte Carlo method as described above. It reproduces the well-known thickness fringes. The peak position is given by the mean displacement,  $\langle V(x, z) \rangle$ . Using Eq. (4), we obtain

$$\begin{aligned} \langle V(x, z) \rangle &= \int_{-\infty}^{\infty} v(x - \xi, z) \langle g(\xi) \rangle d\xi \\ &= \rho \int_{-\infty}^{\infty} v(x, z) dx \\ &= -Qb\rho \left( d - \frac{\nu}{1-\nu} z \right), \end{aligned} \quad (16)$$

where  $\nu$  is the Poisson ratio. As already described in the previous section, we consider only symmetric Bragg reflections,  $\mathbf{Q} = (0, 0, Q)$ , and edge Lomer-type misfit dislocations with the Burgers vector  $\mathbf{b} = (b, 0, 0)$ . The last equality in Eq. (16) is a result of the analytical calculation of the integral with the displacement field of the dislocation parallel to the free surface of an elastic semispace. Since Eq. (16) possesses a linear dependence on  $z$ , the peak position is

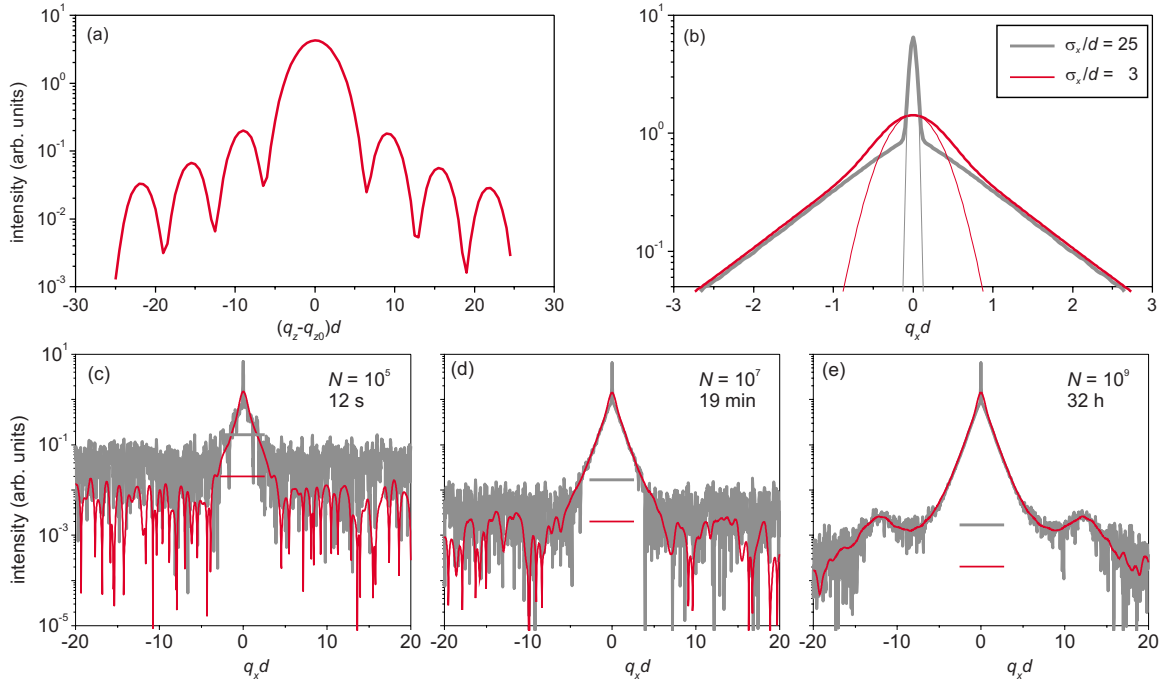


FIG. 2. (Color online) Monte Carlo calculation of the diffraction peaks with low ( $\sigma_x/d=3$ ) and high ( $\sigma_x/d=25$ ) resolutions: (a) the  $q_z$  scan, (b) the central part of the  $q_x$  scan at  $q_z=q_{z0}$ , and (c–e) development of the calculated peak profile with improving data collection statistics. The numbers of generated configurations  $N$  and the CPU time are indicated. The thin lines in (b) show the Gaussian resolution functions. The horizontal bars in (c–e) show the statistical error,  $3\sigma_I/\sqrt{N}$ . The dislocation density is  $\rho d=2$ , the dislocation positions obey a gamma distribution with  $\gamma=25$ .

$$q_{z0} = -\frac{\nu}{1-\nu} Q b \rho. \quad (17)$$

This value is just half of the peak shift due to misfit dislocations [cf. Eq. (10) in Ref. 9], since we consider only dislocations perpendicular to the scattering plane. The dislocations parallel to the scattering plane provide the second half of the peak shift. We do not include them here since they do not influence the peak shapes analyzed below. All  $q_x$  scans are calculated at the peak position  $q_z=q_{z0}$ .

Figures 2(c)–2(e) illustrate an improvement of the calculated peak profile as the number of the generated configurations  $N$  increases. The central peak is resolved with little computational effort, taking just few seconds of CPU time. It takes hours, however, to resolve the satellites. A direct correspondence to the data collection in the experiment is evident: the error decreases as a square root of the number of attempts,  $1/\sqrt{N}$ , like the counting statistics in the experiment. Figures 2(c)–2(e) clearly show that a reduction in the error by one order of magnitude requires the increase in the number of the generated configurations by two orders. In the present paper, we have restricted ourselves with a simple crude Monte Carlo scheme. It can be much improved by more sophisticated versions with variance reduction and quasi-Monte Carlo sequences, see, e.g., Refs. 53–55.

The central regions of the peaks calculated with different resolution are compared in Fig. 2(b). The corresponding Gaussian resolution functions are also shown by thin lines. The high resolution offers the advantage of resolving the coherent peak; other than that, low resolution is sufficient

and allows to save the computation time. Everywhere else, the curves are identical, allowing us to calculate different parts of the peak profiles with different resolutions when appropriate. The low-resolution calculation requires less computation time and can be extended to lower intensities, thus revealing the satellite peaks in Fig. 2(e).

The calculated peak profile in Fig. 2(e) reproduces the main qualitative features of the peaks observed in the experiments discussed in the introduction. The peak consists of a resolution-limited coherent peak due to long-range order and the diffuse intensity caused by the lattice disorder due to dislocations. Since the mean distance between dislocations is  $\rho^{-1}$ , the satellite peaks appear at  $q_x=2\pi\rho m$ , where  $m$  is an integer. The first-order satellites ( $m=\pm 1$ ) are clearly visible in Fig. 2(e), very similar to the experimental observations.<sup>20,21</sup> At small  $q_x$ , the diffuse intensity  $I(q_x)$  is a straight line in the logarithmic plot. This common feature of the experimental curves is well-reproduced in Fig. 2(e).

We investigate the calculated diffraction profiles further in Fig. 3 by varying the relevant parameters in the model. Figure 3(a) shows the variation in the peak shape as a function of the distribution sharpness  $\gamma$ . The case  $\gamma=1$  corresponds to random uncorrelated dislocations and produces a broad Gaussian-shaped peak. As  $\gamma$  is increased, the central coherent peak appears and becomes higher, the satellites appear and increase in intensity, and the central part of the diffuse peak obtains its characteristic exponential shape (straight line in the logarithmic plot).

Figure 3(b) shows the transformation of the peak profile with increased reflection order. We assume the Burgers vector  $b$  equal to the lattice parameter and define the reflection

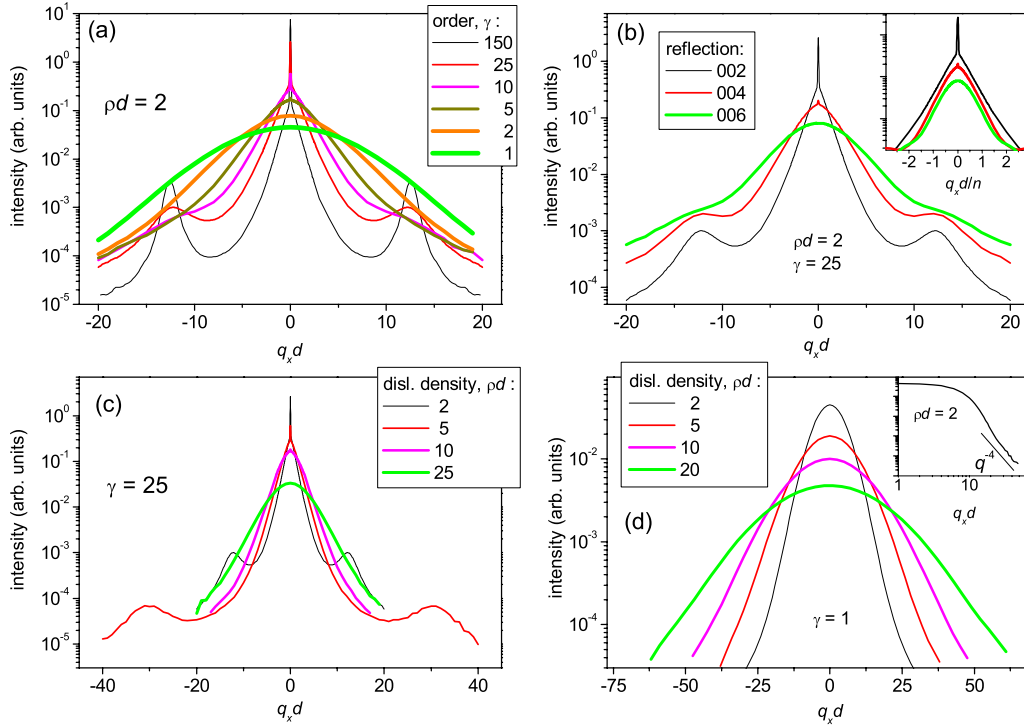


FIG. 3. (Color online) X-ray diffraction peaks calculated by the Monte Carlo method for misfit dislocations forming a Markov chain with the gamma distribution for the distances between subsequent dislocations: variation in the diffraction peaks with changing (a) the order parameter  $\gamma$  of the gamma distribution, (b) the reflection order, (c,d) the dislocation density  $\rho d$  for (c) ordered, and (d) disordered dislocations. The insert in (d) shows the  $q^{-4}$  asymptote of the peak profile.

order as  $n = Qb/2\pi$ . Accordingly, the reflections presented in Fig. 3(b) are  $00n$  reflections. The coherent peak is pronounced for  $n=2$ , becomes weak for  $n=4$ , and disappears at  $n=6$ . The satellites also become weaker and disappear, and the diffuse peak becomes broader. The insert in Fig. 3(b) presents the same curves with the wave vector  $q_x$  scaled by the reflection order. The ratio  $q_x d/n$  is proportional to the angular scale of the transverse scan ( $\omega$  scan) in the experiment. The scaled curves are very close, which reproduces the experimental observation.<sup>39,40</sup> We note that this coincidence of the scaled curves is not universal but takes place only in a limited range of parameters.

Figure 3(c) shows the dislocation density dependence of the peaks for ordered dislocations ( $\gamma=25$ ). As the dislocation density is increased, the satellite peaks become weaker and shift to larger  $q_x$ , according to the formula for their position  $q_x = 2\pi\rho n$ . The coherent peak decreases and disappears, and the peaks assume the Gaussian shape characteristic for large dislocation densities. Figure 3(d) presents similar calculations performed for the case of random uncorrelated dislocations ( $\gamma=1$ ). The Monte Carlo calculation reproduces the features of the peaks that are well-established for uncorrelated dislocations.<sup>9</sup> The peak is Gaussian with a width proportional to  $\sqrt{\rho/d}$ . The insert in Fig. 3(d) shows that the peak has a Gaussian shape only in the central part and reaches the power asymptotic ( $\sim q_x^{-4}$ ) at larger wave vectors, also in a good agreement with the previous study.<sup>56</sup>

Figure 4 explores another type of dislocation correlations. The dislocations are initially placed periodically and then uncorrelated random shifts are added to the positions. Hence,

the dislocation positions are  $\xi_j = j\rho^{-1} + \delta x$ , where  $\delta x$  is a random shift. Figure 4 presents the results obtained for the Gaussian distribution of  $\delta x$  with the standard deviations  $w$  given in units of the mean distance between dislocations  $\rho^{-1}$ . We perform the same study as above for a Markov chain of the dislocation positions. A comparison of Figs. 3(a) and 4(a) clearly shows that the mean periodicity in the dislocation positions results in resolution-limited satellites that do not broaden as the disorder increases. Rather, their intensity decreases.

Another difference seen in Fig. 4(c) is the dislocation density dependence of the diffuse scattering. As the dislocation density is increased in Figs. 4(c) and 4(d), the diffuse intensity decreases, which is opposite to the case of Figs. 3(c) and 3(d). Such a difference can be understood if we take into account that, for a periodic dislocation array, the nonuniform crystal lattice distortions are confined in a layer with a thickness less than the mean distance between dislocations.<sup>23</sup> The disturbance of the periodicity by uncorrelated random shifts of the dislocation positions gives rise to a distorted crystal layer, but its thickness decreases as the dislocation density is increased.

Further insight in the difference between the two types of correlations in the dislocation positions can be achieved by comparing the correlation functions of the dislocation positions. This is done below in Sec. V. It is shown there that the Markov chain gives rise to the short-range correlations exponentially decaying with distance, while the periodic dislocations with random shifts keep the long-range order. The broadened satellites in the first case and the resolution-

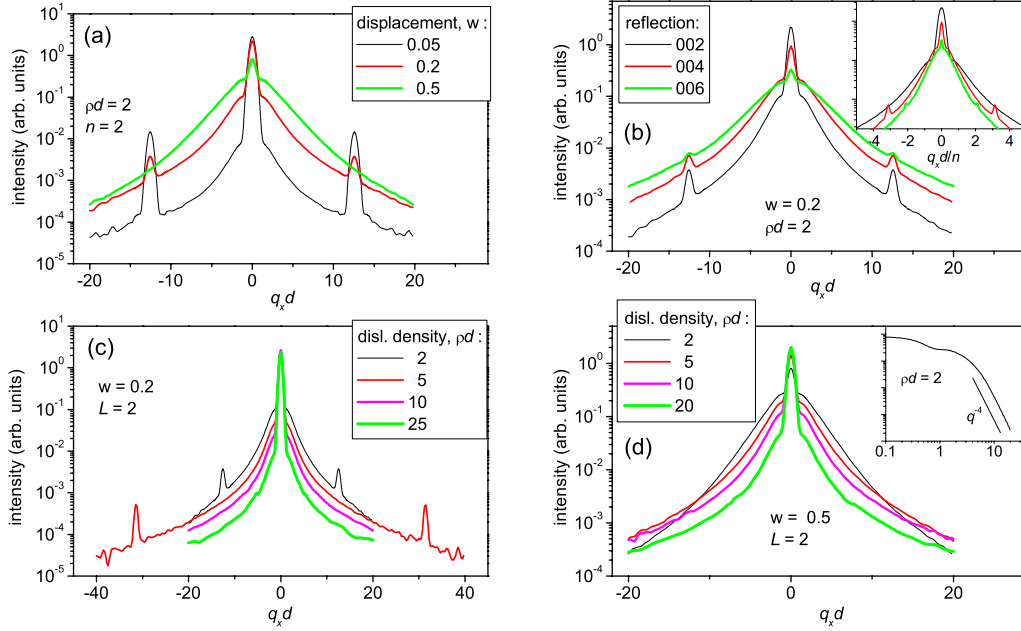


FIG. 4. (Color online) X-ray diffraction peaks calculated by the Monte Carlo method for misfit dislocations with uncorrelated random shifts from a periodic array: variation in the diffraction peaks with changing (a) the width  $w$  of the displacement distribution, (b) the reflection order  $Q$ , (c,d) the dislocation density  $\rho d$  for (c) ordered, and (d) disordered dislocations. The insert in (d) shows the  $q^{-4}$  asymptote of the peak profile.

limited satellites in the second case are due to this difference in the long-range order.

#### IV. PEAK PROFILES FOR GAUSSIAN FLUCTUATIONS

The displacement in the film  $\mathbf{U}(x, z)$  is a random function, since it is the sum of displacements  $\mathbf{u}(x - \xi_j, z)$  from many randomly located dislocations. According to the central limit theorem, the distribution of  $\mathbf{U}(x, z)$  tends to the normal distribution if the number of the dislocations that provide comparable contributions to  $\mathbf{U}(x, z)$  is large enough. This is certainly the case for  $\rho d \gg 1$ . We find, however, that the normal distribution is well-approached already at  $\rho d \geq 1$ : the number of dislocations contributing to  $\mathbf{U}(x, z)$  becomes large enough due to a slow decay of the dislocation displacements with distance  $x$ . Figure 5 presents the probability distribution calculated by the Monte Carlo method for  $\rho d = 2$ . The distribution is already very close to Gaussian.

The normal distribution of the displacements radically simplifies the statistical average (6). We rewrite Eq. (6) as

$$G(x, z_1, z_2) = \langle e^{i[(V_1 - \bar{V}_1) - (V_2 - \bar{V}_2)]} \rangle e^{i(\bar{V}_1 - \bar{V}_2)}. \quad (18)$$

Here, we introduce, in comparison with Eq. (6), the labels 1 and 2 to denote the points  $(x_1, z_1)$  and  $(x_2, z_2)$ , respectively, and subtract the mean values  $\bar{V}_j \equiv \langle V_j \rangle$  from the fluctuating quantities. The aim is to average  $V_i - \bar{V}_i$  with zero mean values. The difference  $V_1 - V_2$  depends on the distance  $x = x_1 - x_2$  only, due to the uniformity of the system in the lateral plane. The difference of the mean values  $\bar{V}_1 - \bar{V}_2$  is equal, according to Eqs. (16) and (17), to  $q z_0(z_1 - z_2)$ . Then, for the normally distributed  $V_i$ 's Eq. (18) reduces to

$$G(x, z_1, z_2) = e^{-T(x, z_1, z_2)} e^{iq z_0(z_1 - z_2)}, \quad (19)$$

where

$$T(x, z_1, z_2) = \frac{1}{2} \langle [(V_1 - \bar{V}_1) - (V_2 - \bar{V}_2)]^2 \rangle. \quad (20)$$

We rewrite the latter expression as

$$T(x, z_1, z_2) = \frac{1}{2} (\langle V_1^2 \rangle - \bar{V}_1^2) + \frac{1}{2} (\langle V_2^2 \rangle - \bar{V}_2^2) - (\langle V_1 V_2 \rangle - \bar{V}_1 \bar{V}_2) \quad (21)$$

and proceed to the evaluation of  $\langle V_1 V_2 \rangle$ , having in mind that the mean squared  $\langle V_1^2 \rangle$  can be directly obtained from it by substituting the coordinates of point 2 by the ones of point 1.

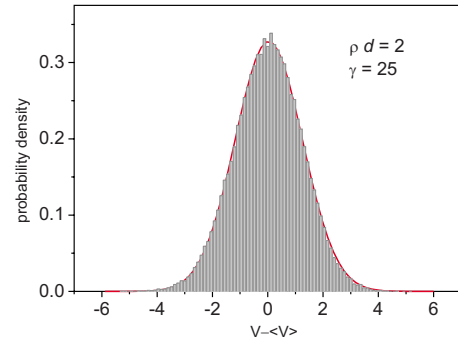


FIG. 5. (Color online) Probability distribution for the displacements obtained by the Monte Carlo calculation (histogram) and a Gaussian fit to it (black line). The displacements are calculated at  $z/d = 0.5$ , the dislocation density  $\rho d = 2$ , the dislocations form a Markov chain with  $\gamma = 25$ .

Using Eq. (4), we represent

$$\langle V_1 V_2 \rangle = \int \int_{-\infty}^{\infty} W(\xi - \xi') v(x_1 - \xi) v(x_2 - \xi') d\xi d\xi', \quad (22)$$

where  $W(\xi - \xi') \equiv \langle g(\xi) g(\xi') \rangle$  is the covariance function of the dislocation positions, and our aim now is to evaluate it. Using Eq. (3), we find

$$\begin{aligned} \langle g(\xi) g(\xi') \rangle &= \int \left\{ \sum_j \delta(\xi - \xi_j) \sum_k \delta(\xi' - \xi_k) \right\} p(\vec{\xi}) d\vec{\xi} \\ &= \sum_j \sum_k \int \delta(\xi - \xi_j) \delta(\xi' - \xi_k) p(\vec{\xi}) d\vec{\xi} \\ &= \sum_j \sum_k \int p(\dots, \xi_j, \dots, \xi'_k, \dots) d\vec{\xi}_{jk}. \end{aligned} \quad (23)$$

Here,  $\vec{\xi} = (\xi_1, \dots, \xi_m, \dots)$  is a sequence of random positions with the constant mean density  $\langle g(\xi) \rangle = \rho$  and the probability density  $p(\vec{\xi})$ , and the notation  $d\vec{\xi}_{jk}$  is used to indicate that the integration over  $d\vec{\xi}$  is carried out over all points excluding  $\xi_j$  and  $\xi_k$ . The arguments  $\xi$  and  $\xi'$  are at the  $j$ th and  $k$ th positions in  $p(\dots, \xi, \dots, \xi', \dots)$ . The last equality in Eq. (23) shows that  $W(\xi - \xi') = \langle g(\xi) g(\xi') \rangle$  is the two-particle probability density to find dislocations at the points  $\xi$  and  $\xi'$ . It depends on the difference  $\xi - \xi'$  due to the stationarity of the random process and consists of a singular part  $\rho \delta(\xi - \xi')$ , arising from the coinciding points  $\xi_j$  and  $\xi_k$  in the sum (23), and a regular part, which is a continuous function of the argument  $\xi - \xi'$

$$W(\xi - \xi') = \rho [\delta(\xi - \xi') + w(\xi - \xi')]. \quad (24)$$

Here,  $w(\xi - \xi')$  is the conditional probability density to find a dislocation at a nonzero distance  $\xi - \xi'$  from the first dislocation, provided the position  $\xi$  is fixed.

When the distance between dislocations increases and their positions decorrelate, the conditional probability  $w$  tends to the mean density  $\rho$ . We denote

$$w(\xi - \xi') = \rho [C(\xi - \xi') + 1], \quad (25)$$

thus introducing the correlation function  $C(x)$  that tends to zero for decorrelated dislocations. This function is evaluated below in Sec. V for different types of correlations. Hence,

$$W(\xi - \xi') = \rho \delta(\xi - \xi') + \rho^2 [C(\xi - \xi') + 1]. \quad (26)$$

It is convenient to Fourier transform the functions involved in Eq. (22),

$$W(x) = \frac{1}{2\pi} \int_{-\infty}^{\infty} W_q e^{iqx} dq, \quad v(x, z) = \frac{1}{2\pi} \int_{-\infty}^{\infty} v_q(z) e^{iqx} dq, \quad (27)$$

and obtain

$$\langle V_1 V_2 \rangle = \frac{1}{2\pi} \int_{-\infty}^{\infty} W_q v_q(z_1) v_q(z_2) e^{iqx} dq. \quad (28)$$

Substituting  $W_q = \rho^2 [C_q + 2\pi \delta(q)] + \rho$  and subtracting the mean values, we arrive at

$$\langle V_1 V_2 \rangle - \bar{V}_1 \bar{V}_2 = \frac{\rho}{\pi} \int_0^{\infty} (\rho C_q + 1) v_q(z_1) v_q(z_2) \cos qx dq. \quad (29)$$

Then, collecting all terms (21), we finally have

$$\begin{aligned} T(x, z_1, z_2) &= \frac{\rho}{2\pi} \int_0^{\infty} dq (\rho C_q + 1) \times [v_q^2(z_1) + v_q^2(z_2) \\ &\quad - 2v_q(z_1) v_q(z_2) \cos qx]. \end{aligned} \quad (30)$$

Equations (5), (19), and (30) present the diffracted intensity in quadratures. Analytical expressions for the function  $C_q$  are derived in the next section for the types of correlations involved in our Monte Carlo calculations.

The only assumption made in the calculations is the normal distribution of the random displacements  $\mathbf{U}(x, z)$ , which is valid under the rather weak restriction  $\rho d \geq 1$ . Then, all correlations are expressed through the pair correlation function  $C(x)$ , since all statistical moments of the Gaussian distribution are uniquely defined by the first two moments, the expectation and the covariance. In his original treatment, Krivoglaz<sup>10,57</sup> avoided the assumption of a normal distribution and used Poisson statistics for the case of uncorrelated dislocations. Applied to the case of uncorrelated misfit dislocations,<sup>9</sup> the correlation function (19) is replaced by

$$G(x, z_1, z_2) = \exp[-\mathcal{T}(x, z_1, z_2)], \quad (31)$$

where

$$\mathcal{T}(x, z_1, z_2) = \rho \int_{-\infty}^{\infty} d\xi \{1 - e^{i[v(\xi, z_1) - v(\xi - x, z_2)]}\}. \quad (32)$$

The power expansion of the exponential function in Eq. (32) to first order gives  $\exp[iq_{z_0}(z_1 - z_2)]$  in Eq. (19) and, to second order, our function  $T(x, z_1, z_2)$  with  $C(x) \equiv 0$ . This expansion assumes that the difference  $v(\xi, z_1) - v(\xi - x, z_2)$  is small, which is approved by the main contribution to the integral from distant dislocations,  $x \gg \xi$ .

Equation (32) can be used in the limit of small dislocation densities,  $\rho \rightarrow 0$ . Then, the exponent in Eq. (31) can be expanded to the first order and the diffracted intensity becomes proportional to the dislocation density. In this limit, the scattering amplitude, Eq. (1), can be written for each dislocation separately. The scattering intensity comes to be the sum of intensities due to different dislocations, since the distance between dislocations tends to infinity and their displacement fields do not overlap. On the other hand, accounting for the correlations in the Krivoglaz approach is fairly complicated, based on the Kubo cumulant expansion.<sup>10</sup> For the normal distribution, the higher-order correlations are expressed through the pair correlations, which allows us to derive the closed formula (30). The normal distribution is approached for sufficiently large dislocation densities and does not allow the limit of small densities.

The expressions for the diffracted intensity can be drastically simplified if the values of the function  $T(x, z_1, z_2)$  do not exceed 1 in the whole range of its arguments. If this condition is satisfied, one can expand  $\exp(-T) \approx 1 - T$ . Although this expansion is possible only in a rather narrow range of parameters specified below, it allows a qualitative

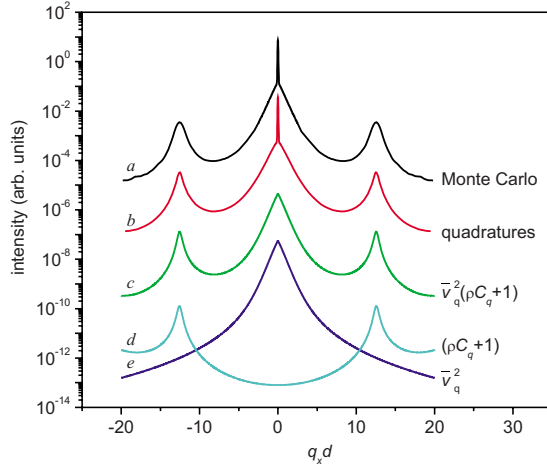


FIG. 6. (Color online) X-ray diffraction peak profiles calculated for  $\rho d=2$ ,  $n=2$ , and  $\gamma=125$ : curve *a* is obtained by the Monte Carlo method, curve *b* by using the quadratures (30), curve *c* by the simplified formulas (33) and (40), curves *d* and *e* demonstrate the contributions to the diffuse intensity due to the correlation term  $\rho C_q+1$  and the dislocation displacement term  $\bar{v}_q^2$ , respectively. The curves are shifted vertically for clarity.

understanding of the components that constitute the peak. The condition  $T \leq 1$  requires first  $\rho d$  to be on the order of 1. If the dislocation density is small, the normal distribution of displacements is not reached and Eq. (19) cannot be used. If the dislocation density is large ( $\rho d \gg 1$ ), the function  $T$  increases proportional to  $\rho d$  and becomes larger than 1. If in addition to  $\rho d \sim 1$  the positional order of dislocations is high enough ( $\gamma \gg 1$  for the Markov chain), the function  $T$  is inversely proportional to  $\gamma$  and the values of  $T$  do not exceed 1 in the whole range of coordinates. Then, the exponential function (19) can be expanded and the integration (5) can be performed analytically.

The expansion  $G(x, z_1, z_2) \approx 1 - T(x, z_1, z_2)$  splits the intensity into the coherent and diffuse parts,  $I = I_{\text{coh}} + I_{\text{diff}}$ . The integration over  $x$  in Eq. (5) of the first constant term gives rise to the delta-function  $\delta(q_x)$ , i.e., it describes the coherent peak. When the finite resolution is taken into account in Eq. (9), the coherent intensity is

$$I_{\text{coh}}(q_x) = \sqrt{2\pi} d^2 \mathcal{R}(q_x). \quad (33)$$

The diffuse intensity is obtained, according to Eq. (5), as the Fourier transform of  $T(x, z_1, z_2)$ , which itself is given by a Fourier integral (30). This results in a simple formula

$$I_{\text{diff}}(q_x) = \rho \bar{v}_q^2 (\rho C_q + 1). \quad (34)$$

Here, we have defined  $\bar{v}_q = \int_0^d v_q(z) dz$  and assumed that the resolution is good enough, so that the diffuse intensity distribution is much broader than the resolution function. The analytical expression for  $\bar{v}_q$  is given in the Appendix, see Eq. (A9).

Figure 6 compares the diffraction peak profiles calculated by different methods and in different approximations for one and same set of parameters. Curve *a* is similar to the curves in Fig. 3(a). It is calculated by the Monte Carlo method for a

dislocation array forming a Markov chain with  $\gamma=125$ . Curve *b* shows the results of a numerical integration by Eqs. (5), (19), and (30). It uses the Fourier transformed correlation function  $C_q$  obtained below, see Eq. (37). The good agreement of curves *a* and *b* demonstrates that the approximation of a Gaussian distribution of the total displacements is applicable. We have performed a similar comparison (not shown here) of the results of the Monte Carlo calculations and the numerical integration and found that they agree in a wide range of parameters. The diffuse intensity calculated by Eq. (40) is shown by curve *c*. This simplified formula has a narrow applicability range, as discussed above. However, it allows us to single out two main components determining the peak profile. One can see that the displacement fields of the individual dislocations (Fourier transformed over  $x$  and integrated over  $z$  to obtain  $w_q$ ) define the diffuse scattering in the vicinity of the coherent peak. The dislocation correlations only weakly influence this region. They determine the satellite peaks at the positions where the dislocation displacement term  $w_q$  smoothly varies. Such decomposition of the diffraction peaks is quantitatively correct only for  $\gamma \gg 1$ , but qualitatively can be applied to understand the formation of the peak profiles at smaller  $\gamma$  in Fig. 3 as well.

## V. CORRELATION FUNCTIONS OF DISLOCATION POSITIONS

### A. Markov chain of positions

We consider, as in the Monte Carlo calculations above, a Markov chain of dislocation positions with a probability density  $p(x)$  of a distance  $x$  between two subsequent dislocations. Our aim is to calculate the conditional probability  $w(x)$  to find a dislocation at the position  $x$ , provided there is a dislocation at the origin. We consider first  $x > 0$  and introduce a function  $\tilde{w}(x) = w(x)\theta(x)$ , where  $\theta(x)$  is equal to 1 for  $x > 0$  and 0 for  $x < 0$ . The probability that the next dislocation is at distance  $x$  from the origin is  $p(x)$ . The probability of a dislocation at  $x$  with an intermediate dislocation in between is  $\int_0^x p(\xi)p(x-\xi)d\xi$ . Although this integral is written with an infinite upper limit, the actual integration range is  $0 \leq \xi \leq x$ , since the probability  $p(x)$  is identically equal to zero for  $x < 0$ . Continuing to the general case of  $n-1$  dislocations in between, we arrive at

$$\begin{aligned} \tilde{w}(x) = & p(x) + \int_0^x p(\xi)p(x-\xi)d\xi \\ & + \int \int_0^x p(\xi)p(\xi')p(x-\xi-\xi')d\xi d\xi' + \dots \end{aligned} \quad (35)$$

This equation can be written as

$$\tilde{w}(x) = p(x) + \int_0^x \tilde{w}(\xi)p(x-\xi)d\xi. \quad (36)$$

Fourier transforming this equation and using the convolution formula, we obtain, for  $q \neq 0$ ,  $\tilde{w}_q = p_q + p_q \tilde{w}_q$ , and, therefore,  $\tilde{w}_q = p_q / (1 - p_q)$ . Now, we take into account that the function  $w(x)$  is even for the stationary process and  $w(x) = \tilde{w}(x) + \tilde{w}(-x)$ . Then,

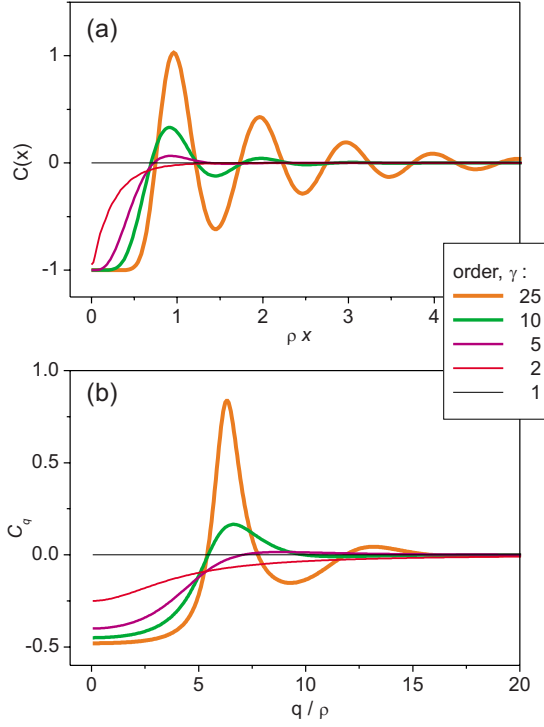


FIG. 7. (Color online) (a) Correlation function of dislocation positions  $C(x)$  and (b) its Fourier transform  $C_q$  for dislocations forming a Markov chain, with the gamma distribution for the distances between dislocations. The values of its parameter  $\gamma$  are indicated.

$$C_q = \frac{2}{\rho} \operatorname{Re} \frac{p_q}{1 - p_q}, \quad (37)$$

and the correlation function  $C(x)$  is expressed finally as

$$C(x) = \frac{2}{\pi\rho} \int_0^\infty \operatorname{Re} \frac{p_q}{1 - p_q} \cos qx dq. \quad (38)$$

For the gamma distribution (15), the Fourier transformation of the probability density can be performed analytically,

$$p_q = \frac{1}{[1 + iq/\gamma\rho]^\gamma}. \quad (39)$$

Figure 7 shows the correlation function (38) and its Fourier transform (37). We also calculated  $C(x)$  by the Monte Carlo method, by generating dislocation arrays and counting the probability to find two dislocations separated by a given distance  $x$ . The results of both calculations coincide. The case  $\gamma=1$  corresponds to an exponential distribution of distances between dislocations and the absence of correlations,  $C(x)=0$ . As  $\gamma$  is increased, the order of dislocations progressively increases.  $C(x)$  becomes close to  $-1$  for small  $x$ , which corresponds to a low probability  $\rho[C(x)+1]$  to find two dislocations very close to each other. This probability is maximum at multiples of the mean distance between dislocations, with the maximum values decaying with increasing  $x$ . The curves in Fig. 7(a) are characteristic for short-range order.

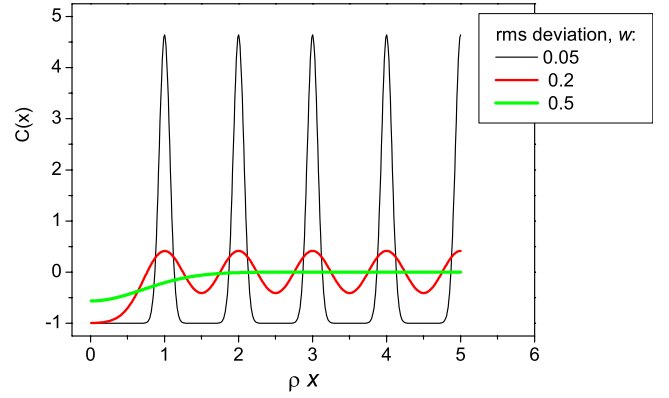


FIG. 8. (Color online) Correlation function of dislocation positions  $C(x)$  for dislocations with random uncorrelated shifts from an initially periodic array. Gaussian distribution of random shifts, the standard deviations  $w$  are given in units of the mean distance between dislocations.

Accordingly, they give rise to the finite-width peaks in  $C_q$ . These peaks become higher and sharper as  $\gamma$  is increased. They define the satellites in Figs. 3 and 6.

### B. Periodic dislocations with uncorrelated random positional shifts

Let us now calculate the correlation function for dislocations with random uncorrelated shifts from initial periodic positions. Consider two dislocations, with the initial positions 0 and  $\xi_j = j\rho^{-1}$ . Here  $j$  is an integer, and  $j \neq 0$  since we consider two different dislocations. As a result of the shift, the first dislocation takes a random position  $\xi$  with the probability  $p(\xi)$  and the second one a position  $\xi'$  with the probability  $p(\xi' - \xi_j)$ . The probability of a distance  $x = \xi - \xi'$  between these dislocations is equal to  $\int_{-\infty}^\infty p(\xi)p(\xi - x - \xi_j)d\xi$ . The sum of these probabilities over all dislocations is equal to  $w(x)$ . Hence, we have

$$w(x) = \sum_{\substack{j=-\infty \\ j \neq 0}}^{\infty} \int_{-\infty}^{\infty} p(\xi)p(\xi - x - \xi_j)d\xi. \quad (40)$$

The Monte Carlo calculations in Fig. 4 are performed for a Gaussian probability distribution with the standard deviation  $w$ , i.e.,  $p(x) = (\sqrt{2\pi}w)^{-1} \exp[-\frac{1}{2}(x/w)^2]$ . Then, the integrals in Eq. (40) can be calculated analytically and we obtain

$$C(x) + 1 = \sum_{\substack{j=-\infty \\ j \neq 0}}^{\infty} \frac{1}{2\sqrt{\pi\rho w}} \exp\left[-\left(\frac{x - j\rho^{-1}}{2w}\right)^2\right]. \quad (41)$$

Figure 8 presents the functions  $C(x)$  calculated by Eq. (41). We have also obtained these functions by a direct Monte Carlo calculation, and found a coincidence of the results. Similar to the Markov chain case in Fig. 7(a),  $C(x)$  is close to  $-1$  at small  $x$  and has maxima at positions corresponding to the mean distances between dislocations. In contrast to the former case, however, the maximum values do not decrease as the distance  $x$  increases. This long-range or-

der results in the delta functions in  $C_q$  and in the resolution-limited satellite peaks in Fig. 4. The Fourier transform of Eq. (41) is

$$C_q = 2\pi\rho^{-1}e^{-(wq)^2} \left[ \sum_{\substack{k=-\infty \\ k \neq 0}}^{\infty} \rho\delta(q - 2\pi\rho k) - 1 \right]. \quad (42)$$

### C. Periodic dislocations with correlated positional shifts

In the analysis above, we have generated correlated random positions for dislocations in two different intuitively evident ways, either as a Markov chain or providing uncorrelated random shifts from periodic positions. The correlation functions  $C(x)$  were calculated afterwards. It may be instructive to approach the problem of correlated dislocations in the opposite direction: let us produce correlated shifts from the periodic initial positions with a correlation function for the shifts that is given in advance. A method for the generation of such a dislocation distribution is proposed below. As an additional advantage, this method requires just a few random numbers to generate a set of dislocations, irrespective of the number of dislocations in the set. However, it is not as intuitive as the methods described above.

Let us start with a periodic dislocation array,  $x_j = j\rho^{-1}$ , and define shifts  $\delta x_j$  of these positions according to the formula

$$\delta x_j = w(\eta_1 \cos \tau x_j + \eta_2 \sin \tau x_j). \quad (43)$$

Here,  $\eta_1$  and  $\eta_2$  are two independent random variables, the same for all  $j$ , possessing the standard Gaussian distribution with zero mean value, and  $\tau$  is another random variable also sampled once for all  $j$  independent of  $\eta_1$  and  $\eta_2$ . The probability density  $p(\tau)$  is not specified yet, and  $w$  is a constant that also remains to be defined. It is the rms of the random shifts  $\delta x_j$ , i.e.,  $w^2 = \langle (\delta x_j)^2 \rangle$ . We introduce the correlation function for the shifts  $B(x) = \langle \delta x_i \delta x_j \rangle$ , where  $x = x_i - x_j$ . Its calculation is straightforward, taking into account that  $\langle \eta_1^2 \rangle = \langle \eta_2^2 \rangle = 1$ ,  $\langle \eta_1 \eta_2 \rangle = 0$ , and  $B(-x) = B(x)$

$$\begin{aligned} B(x) = \langle \delta x_i \delta x_j \rangle &= w^2 \int_0^\infty (\langle \eta_1^2 \rangle \cos \tau x_i \cos \tau x_j \\ &\quad + \langle \eta_2^2 \rangle \sin \tau x_i \sin \tau x_j) p(\tau) d\tau \\ &= w^2 \int_0^\infty p(\tau) \cos \tau x d\tau. \end{aligned} \quad (44)$$

Hence, the probability density  $p(\tau)$  is the spectral function of  $w^{-2}B(x)$ ,

$$p(\tau) = \frac{2}{\pi w^2} \int_0^\infty B(x) \cos \tau x dx, \quad (45)$$

and the constant  $w$  is obtained from the normalization condition  $\int_0^\infty p(\tau) d\tau = 1$ , which gives  $w^2 = B(0)$ .

For example, if the target correlation function has a Lorentzian form,

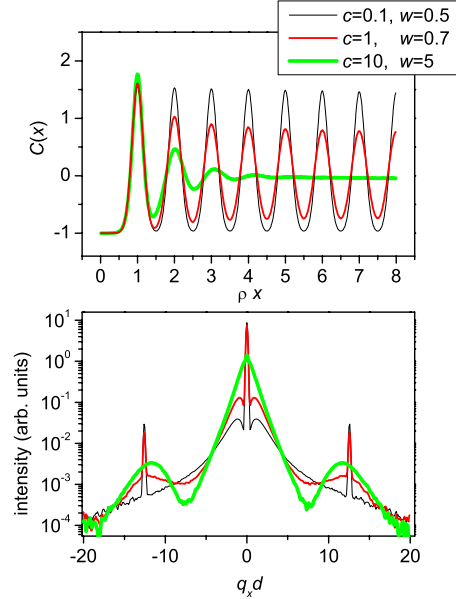


FIG. 9. (Color online) (a) Correlation functions for dislocation positions  $C(x)$  and (b) the calculated diffraction peaks for dislocations with the shifts from an initially periodic array correlated by Eq. (46). The parameter  $c$  for the random variable  $\tau$  and the standard deviation  $w$  for Gaussian random variables  $\eta_1, \eta_2$  in Eq. (43) are given.

$$B(x) = \frac{w^2}{1 + (x/c)^2}, \quad (46)$$

where the constant  $c$  is a correlation length scale, then the probability density has the form  $p(\tau) = c \exp(-c\tau)$ . It is simulated as  $\tau = -\log(\text{rand})/c$ , where  $\text{rand}$  is a random number from a uniform distribution on the interval  $[0,1]$ .<sup>52</sup> As another example, the exponential correlation function

$$B(x) = c \exp(-cx) \quad (47)$$

has a Lorentzian spectrum, which is simulated as  $\tau = c \tan[\pi(2\text{rand}-1)/2]$ .<sup>52</sup>

We improve the ergodic properties of the random process (43) by averaging over a large number of independent processes (typically, we take 20 terms). This also ensures (by the central limit theorem) that the random process  $\delta x_j$  has a multidimensional Gaussian distribution. In contrast to single control parameter of the correlation functions in Secs. V A and V B, we can now independently vary two parameters, namely, the standard deviation  $w$  of random shifts  $\delta x_j$  and the decorrelation parameter  $c$  in Eqs. (46) and (47). Figure 9(a) illustrates a variety of correlation functions for the dislocation positions  $C(x)$  that can be obtained with the Lorentzian function  $B(x)$ , Eq. (46). The curves are obtained by a direct Monte Carlo calculation. They show the correlation functions which have the same first oscillations but different decay with increasing distance  $x$ . Figure 9(b) presents the diffraction profiles obtained for these correlation functions. Faster decay of the correlations results in larger diffuse scattering and broadening of satellite reflections.

## VI. CONCLUSIONS

We have proposed a Monte Carlo method to calculate the x-ray diffraction peaks from crystals with arbitrarily correlated crystal lattice defects. The method is formulated on the example of misfit dislocations and triple crystal diffractometry but it is equally applicable to any other geometry of dislocations and diffraction experiment. In this method, both spatial integration and the average over dislocation statistics are performed simultaneously by the Monte Carlo technique. The distribution of spatial points in the integration is dictated by the experimental resolution. Different parts of a diffraction curve can be obtained with different resolution and then combined. The results of the calculations explain the diffraction peak profiles observed in various epitaxial systems with a misfit of a few percent and film thicknesses of several tens of nanometers.<sup>20,21,26–46</sup>

The displacements of atoms in the film are sums of the contributions from the dislocation displacement fields and can be considered as random functions of the dislocation positions. If the mean distance between dislocations is smaller than the film thickness, the displacements possess the normal distribution, due to contributions from a sufficiently large number of dislocations. In this case, the diffracted intensity can be expressed in quadratures through the correlation function of the dislocation positions. We have proposed different types of the correlation functions and obtain diffraction peak profiles for them.

## ACKNOWLEDGMENTS

The authors thank Oliver Brandt and Henning Riechert for useful discussions. The financial support from RFBR under Grant Nos. 09-01-00152-a and 09-01-12028-ofi-m is kindly acknowledged.

## APPENDIX: DISPLACEMENT DUE TO A DISLOCATION PARALLEL TO THE SURFACE OF HALF-SPACE

The  $z$  component of the displacement  $\mathbf{u}(x, z)$  due to an edge dislocation with the Burgers vector  $\mathbf{b}=(b_x, 0, 0)$  parallel to the surface of an elastically isotropic half-space can be written as a sum of three terms,<sup>9,51</sup>

$$u_z(x, z) = u_{z1} + u_{z2} + u_{z3}. \quad (\text{A1})$$

The sum consists of the dislocation displacement in the infinite medium

$$u_{z1} = \frac{b_x}{2\pi} \left[ \frac{1-\alpha}{2} \ln(x^2 + (z-d)^2) + \frac{\alpha x^2}{x^2 + (z-d)^2} \right], \quad (\text{A2})$$

the image dislocation

$$u_{z2} = -\frac{b_x}{2\pi} \left[ \frac{1-\alpha}{2} \ln(x^2 + (z+d)^2) + \frac{\alpha x^2}{x^2 + (z+d)^2} \right], \quad (\text{A3})$$

and the additional relaxation term

$$u_{z3} = -\frac{b_x d}{\pi} \left[ \frac{z+d}{x^2 + (z+d)^2} + \frac{\alpha z((z+d)^2 - x^2)}{(x^2 + (z+d)^2)^2} \right]. \quad (\text{A4})$$

Here,  $\alpha=1/[2(1-\nu)]$ , where  $\nu$  is the Poisson ratio. We take  $\nu=1/3$ .

The Fourier transform of  $u_z(x, z)$  over the coordinate  $x$  can be calculated analytically

$$u_q(z) = u_{1q} + u_{2q} + u_{3q}, \quad (\text{A5})$$

where

$$u_{1q}(z) = \frac{b_x}{2q} e^{-q(d-z)} \{1 - \alpha[1 - q(d-z)]\}, \quad (\text{A6})$$

$$u_{2q}(z) = -\frac{b_x}{2q} e^{-q(d+z)} \{1 - \alpha[1 - q(d+z)]\}, \quad (\text{A7})$$

$$u_{3q}(z) = b_x d e^{-q(d+z)} (1 + \alpha q z). \quad (\text{A8})$$

In Eq. (40), we also need the integral over  $z$ ,  $\bar{v}_q = \int_0^d v_q(z) dz$ , which is

$$\bar{v}_q = -\frac{Q_z b_x}{2q^2} \{1 - 2(1 - qd)e^{-qd} + [1 - 2qd(1 + \alpha qd)]e^{-2qd}\}. \quad (\text{A9})$$

<sup>1</sup>J. W. Matthews and A. E. Blakeslee, *J. Cryst. Growth* **27**, 118 (1974).  
<sup>2</sup>J. R. Willis, S. C. Jain, and R. Bullough, *Philos. Mag. A* **62**, 115 (1990).  
<sup>3</sup>R. Hull and J. C. Bean, *Crit. Rev. Solid State Mater. Sci.* **17**, 507 (1992).  
<sup>4</sup>S. C. Jain, A. H. Harker, and R. A. Cowley, *Philos. Mag. A* **75**, 1461 (1997).  
<sup>5</sup>A. Trampert and K. H. Ploog, *Cryst. Res. Technol.* **35**, 793 (2000).  
<sup>6</sup>S. N. G. Chu, A. T. Macrander, K. E. Stege, and W. D. Johnston, *J. Appl. Phys.* **57**, 249 (1985).

<sup>7</sup>H. Heinke, M. O. Möller, D. Hommel, and G. Landwehr, *J. Cryst. Growth* **135**, 41 (1994).  
<sup>8</sup>U. Pietsch, V. Holý, and T. Baumbach, *High-Resolution X-Ray Scattering: From Thin Films to Lateral Nanostructures* (Springer-Verlag, Berlin, 2004).  
<sup>9</sup>V. M. Kaganer, R. Köhler, M. Schmidbauer, R. Opitz, and B. Jenichen, *Phys. Rev. B* **55**, 1793 (1997).  
<sup>10</sup>M. A. Krivoglaz, *X-Ray and Neutron Diffraction in Nonideal Crystals* (Springer-Verlag, Berlin, 1996).  
<sup>11</sup>M. A. Krivoglaz and K. P. Ryboshapka, *Fiz. Met. Metalloved.* **15**, 18 (1963) [*Phys. Met. Metallogr.* **15**, 14 (1963)].  
<sup>12</sup>M. Wilkens, *Phys. Status Solidi A* **2**, 359 (1970).

- <sup>13</sup>M. Wilkens, *Krist. Tech.* **11**, 1159 (1976).
- <sup>14</sup>M. A. Krivoglaz, O. V. Martynenko, and K. P. Ryboshapka, *Fiz. Met. Metalloved.* **55**, 5 (1983).
- <sup>15</sup>V. M. Kaganer, O. Brandt, A. Trampert, and K. H. Ploog, *Phys. Rev. B* **72**, 045423 (2005).
- <sup>16</sup>S. Daniš, V. Holý, Z. Zhong, G. Bauer, and O. Ambacher, *Appl. Phys. Lett.* **85**, 3065 (2004).
- <sup>17</sup>S. Daniš and V. Holý, *J. Alloys Compd.* **401**, 217 (2005).
- <sup>18</sup>A. Bourret and P. H. Fuoss, *Appl. Phys. Lett.* **61**, 1034 (1992).
- <sup>19</sup>G. Renaud, P. Guénard, and A. Barbier, *Phys. Rev. B* **58**, 7310 (1998).
- <sup>20</sup>A. Yu. Babkevich, R. A. Cowley, N. J. Mason, and A. Stunault, *J. Phys.: Condens. Matter* **12**, 4747 (2000).
- <sup>21</sup>A. Yu. Babkevich, R. A. Cowley, N. J. Mason, S. Weller, and A. Stunault, *J. Phys.: Condens. Matter* **14**, 13505 (2002).
- <sup>22</sup>R. Popescu, H. L. Meyerheim, D. Sander, J. Kirschner, P. Steadman, O. Robach, and S. Ferrer, *Phys. Rev. B* **68**, 155421 (2003).
- <sup>23</sup>D. K. Satapathy, V. M. Kaganer, B. Jenichen, W. Braun, L. Däw-eritz, and K. H. Ploog, *Phys. Rev. B* **72**, 155303 (2005).
- <sup>24</sup>T. Schmidt, R. Kröger, J. I. Flege, T. Clausen, J. Falta, A. Janzen, P. Zahl, P. Kury, M. Kammler, and M. Horn-von Hoegen, *Phys. Rev. Lett.* **96**, 066101 (2006).
- <sup>25</sup>A. Shalimov, J. Bak-Misiuk, V. M. Kaganer, M. Calamitoutou, and A. Georgakilas, *J. Appl. Phys.* **101**, 013517 (2007).
- <sup>26</sup>P. M. Reimer, H. Zabel, C. P. Flynn, and J. A. Dura, *Phys. Rev. B* **45**, 11426 (1992).
- <sup>27</sup>P. M. Reimer, H. Zabel, C. P. Flynn, and J. A. Dura, *J. Cryst. Growth* **127**, 643 (1993).
- <sup>28</sup>D. F. McMorrow, R. A. Cowley, A. Gibaud, R. C. C. Ward, and M. R. Wells, *Appl. Phys. Lett.* **63**, 2195 (1993).
- <sup>29</sup>A. Gibaud, R. A. Cowley, D. F. McMorrow, R. C. C. Ward, and M. R. Wells, *Phys. Rev. B* **48**, 14463 (1993).
- <sup>30</sup>A. Stierle, A. Abromeit, N. Metoki, and H. Zabel, *J. Appl. Phys.* **73**, 4808 (1993).
- <sup>31</sup>A. Gibaud, D. F. McMorrow, and P. P. Swaddling, *J. Phys.: Condens. Matter* **7**, 2645 (1995).
- <sup>32</sup>C. Sürgers, C. Strunk, and H. v. Löhneysen, *Thin Solid Films* **239**, 51 (1994).
- <sup>33</sup>M. Huth and C. P. Flynn, *Appl. Phys. Lett.* **71**, 2466 (1997).
- <sup>34</sup>A. R. Wildes, R. A. Cowley, R. C. C. Ward, M. R. Wells, C. Jansen, L. Wiren, and J. P. Hill, *J. Phys.: Condens. Matter* **10**, L631 (1998).
- <sup>35</sup>G. L. Zhou and C. P. Flynn, *Phys. Rev. B* **59**, 7860 (1999).
- <sup>36</sup>B. Wölfling, K. Theis-Bröhl, C. Sutter, and H. Zabel, *J. Phys.: Condens. Matter* **11**, 2669 (1999).
- <sup>37</sup>A. Remhof, G. Song, C. Sutter, A. Schreyer, R. Siebrecht, H. Zabel, F. Güthoff, and J. Windgasse, *Phys. Rev. B* **59**, 6689 (1999).
- <sup>38</sup>A. R. Wildes, J. Mayer, and K. Theis-Bröhl, *Thin Solid Films* **401**, 7 (2001).
- <sup>39</sup>P. F. Miceli and C. J. Palmstrøm, *Phys. Rev. B* **51**, 5506 (1995).
- <sup>40</sup>P. F. Miceli, J. Weatherwax, T. Krentsel, and C. J. Palmstrøm, *Physica B* **221**, 230 (1996).
- <sup>41</sup>A. G. Zaitsev, G. Ockenfuss, D. Guggi, R. Wördenweber, and U. Krüger, *J. Appl. Phys.* **81**, 3069 (1997).
- <sup>42</sup>M. Becht, F. Wang, J. G. Wen, and T. Morishita, *J. Cryst. Growth* **170**, 799 (1997).
- <sup>43</sup>X. Castel, M. Guilloux-Viry, A. Perrin, J. Lesueur, and F. Falu, *J. Cryst. Growth* **187**, 211 (1998).
- <sup>44</sup>A. Boule, R. Guinebretière, and A. Dager, *J. Appl. Phys.* **97**, 073503 (2005).
- <sup>45</sup>S. Gariglio, N. Stucki, J.-M. Triscone, and G. Triscone, *Appl. Phys. Lett.* **90**, 202905 (2007).
- <sup>46</sup>D. Kwon, B. Kim, P. Tong, and B. G. Kim, *Appl. Phys. Lett.* **93**, 042902 (2008).
- <sup>47</sup>R. I. Barabash, W. Donner, and H. Dosch, *Appl. Phys. Lett.* **78**, 443 (2001).
- <sup>48</sup>K. K. Sabelfeld, *Monte Carlo Methods in Boundary Value Problems* (Springer, New York, 1991).
- <sup>49</sup>V. M. Kaganer, O. Brandt, H. Riechert, and K. K. Sabelfeld, *Phys. Rev. B* **80**, 033306 (2009).
- <sup>50</sup>V. Holý, T. Baumbach, D. Lübbert, L. Helfen, M. Ellyan, P. Mikulík, S. Keller, S. P. DenBaars, and J. Speck, *Phys. Rev. B* **77**, 094102 (2008).
- <sup>51</sup>J. Lothe, in *Elastic Strain Fields and Dislocation Mobility*, edited by V. L. Indenbom and J. Lothe (North-Holland, Amsterdam, 1992), Chap. 5.
- <sup>52</sup>W. H. Press, S. A. Teukolsky, W. T. Vetterling, and B. P. Flannery, *Numerical Recipes in Fortran 77: The Art of Scientific Computing*, 2nd ed. (Cambridge University Press, Cambridge, England, 1992), Vol. 1, Chap. 7.
- <sup>53</sup>J. M. Hammersley and D. C. Handscomb, *Monte Carlo Methods* (Chapman and Hall, London, 1964).
- <sup>54</sup>H. Niederreiter, *Random Number Generation and Quasi-Monte Carlo Methods* (SIAM, Philadelphia, 1992).
- <sup>55</sup>G. A. Mikhailov, *Optimization of Weighted Monte Carlo Methods* (Springer, New York, 1992).
- <sup>56</sup>V. M. Kaganer, A. Shalimov, J. Bak-Misiuk, and K. H. Ploog, *J. Phys.: Condens. Matter* **18**, 5047 (2006).
- <sup>57</sup>M. A. Krivoglaz, *Fiz. Met. Metalloved.* **12**, 465 (1961).